Neuronal firing modulation by a membrane-targeted photoswitch

Mattia Lorenzo DiFrancesco [1,2,13], Francesco Lodola [3,13], Elisabetta Colombo[1,2,13], Luca Maragliano[1,2], Mattia Bramini [1,2,10], Giuseppe Maria Paternò [3], Pietro Baldelli[2,4], Mauro Dalla Serra [5,6], Lorenzo Lunelli[5,6], Marta Marchioretto[5,6], Giorgio Grasselli [1,2], Simone Cimò[3,7], Letizia Colella[7], Daniele Fazzi[8], Fausto Ortica[9], Vito Vurro[3], Cyril Giles Eleftheriou[1,2,11], Dmytro Shmal [1,2], José Fernando Maya-Vetencourt[1,2,12], Chiara Bertarelli[3,7,13], Guglielmo Lanzani [3,13]★ and Fabio Benfenati [1,2,13]★

Optical technologies allowing modulation of neuronal activity at high spatio-temporal resolution are becoming paramount in neuroscience. In this respect, azobenzene-based photoswitches are promising nanoscale tools for neuronal photostimulation. Here we engineered a light-sensitive azobenzene compound (Ziapin2) that stably partitions into the plasma membrane and causes its thinning through *trans*-dimerization in the dark, resulting in an increased membrane capacitance at steady state. We demonstrated that in neurons loaded with the compound, millisecond pulses of visible light induce a transient hyperpolarization followed by a delayed depolarization that triggers action potential firing. These effects are persistent and can be evoked in vivo up to 7 days, proving the potential of Ziapin2 for the modulation of membrane capacitance in the millisecond timescale, without directly affecting ion channels or local temperature.

O ptical technologies for the modulation of neuronal activity are becoming increasingly important in cell biology and neuroscience[1,2]. Indeed, the possibility to obtain neuronal excitation or inhibition on demand not only has allowed an unprecedented power in interrogating and dissecting out the function of specific brain circuits, but also has opened new perspectives for treating neurological and psychiatric diseases[3].

Optogenetics is the pioneering technique in neuro-optical technologies[3,4]. Similar to optogenetics, the generation of tethered azobenzene photoswitches targeted to membrane bilayers[5–10] or linked to ion channels[11–16] allowed modulating ion channel dynamics and/or the electrical properties of the membrane in a light-dependent fashion.

Extracellular photostimulation by light-sensitive interfaces represents an alternative strategy. Extended planar organic interfaces were used to achieve light-dependent modulation of the electrical state of neurons[17–21] that, at high light intensities, also involved a thermal effect[19,22,23]. Similar results were obtained by increasing the local temperature with infrared illumination of absorbers in contact with cells[24,25], thus increasing the membrane capacitance and in turn depolarizing the target cell. However, temperature rises of several degrees can be harmful to neurons, particularly if administered repeatedly.

In this work, we engineered an amphiphilic azobenzene-based photoswitch to obtain an intramembrane actuator for inducing heatless membrane stress/perturbation upon irradiation with visible light. Our photochromic actuator, named Ziapin2, contains two ionic-terminated alkyl chains that align with the phospholipid headgroups and the azobenzene moiety end-capped with a hydrophobic azepane that can be folded/unfolded in a light-dependent manner. Incubation of the compounds with primary neurons showed that the molecules spontaneously partition into the membrane, where they preferentially distribute to membrane rafts and induce membrane thinning and increased capacitance through *trans*-dimerization. *Trans*→*cis* isomerization triggered by millisecond pulses of visible light displaces the hydrophobic end group from the membrane core and causes a sharp and transient decrease in capacitance due to membrane relaxation that generates a transient hyperpolarization. In neurons, the fast return of capacitance to the steady-state level is followed by action potential (AP) firing. Persistent light-evoked stimulation of Ziapin2-labelled mouse somatosensory cortex activity is also observed in vivo.

Synthesis and characterization of Ziapin2

Amphiphilic azobenzenes have been previously reported for different applications[5]. Herein, we were inspired by the initial work of Fujiwara and Yonezawa, who showed that an aliphatic amphiphilic azobenzene derivative was able to change the capacitance of black lipid membranes in response to prolonged ultraviolet (UV)

illumination[6–8], and by the subsequent work of Bazan and collaborators, who reported that non-photochromic water-soluble distyrylstilbene oligoelectrolytes (DSSN+), capped at each end with nitrogen-bound terminally charged pendant groups, effectively localized to the membrane, modifying its optical and electronic properties[9,10]. Here, we combined a hydrophobic backbone containing the photoactive 4-4′ diaminoazobenzene substituted on one side with an azepane and on the opposite side with alkyl chains that are ω-substituted with cationic groups, that is, pyridinium salts. The combination of the alkyl-substituted azobenzenes with a capping cation leads to amphiphilic species able to dwell inside the cell membrane (Ziapin2; Supplementary Fig. 1 and Methods).

Azobenzene molecules undergo *trans*→*cis* isomerization upon illumination with visible radiation (Fig. 1a), with the reverse *cis*→*trans* isomerization driven by either light or thermal excitation[26–28]. Ziapin2 shows the typical UV–visible (Vis) absorption features of para amino-substituted azobenzenes, with a strong absorption peak centred at 470 nm (Fig. 1b), attributed to the π→π* transitions of the *trans* isomer[28]. Irradiation with blue light leads to *trans*→*cis* isomerization as seen from the concomitant bleaching of the *trans* isomer absorption and increase of the *cis* conformer absorption. A well-defined and relatively fast collective photoswitching dynamics of Ziapin2 in dimethyl sulphoxide (DMSO) was detected by measuring the decrease of absorbance at 470 nm versus irradiation time (Fig. 1c). The steep time-dependent decrease in Ziapin2 photoluminescence (PL) at 540 nm in DMSO upon blue light exposure (Fig. 1d,e) can also be related to the photoisomerization-induced reduction in the *trans* population due to the negligible PL quantum yield of the *cis* isomer. Indeed, the excitation profile of the normalized change in PL (Supplementary Fig. 2a,b) follows the absorption profile of the *trans* isomer, confirming its relation to the isomerization process. We estimated a *trans*→*cis* photoisomerization coefficient $k\tau = 16.9\,\text{cm}^2\,\text{J}^{-1}$ and a *cis*→*trans* thermal rate $y = 0.06\,\text{s}^{-1}$ (red line in Fig. 1e; see Methods). A complete suppression of the Ziapin2 photoswitching was observed in water as compared with DMSO (Fig. 1f), likely caused by strong aggregation of Ziapin2[29]. The formation of aggregates was also corroborated by the redshift of Ziapin2 PL (82 nm, Supplementary Fig. 2c,d) and absorption (22 nm, Supplementary Fig. 2e) in water. To disentangle a possible fast relaxation behaviour from a complete isomerization suppression of Ziapin2 in water, we carried out time-resolved PL measurements in the picosecond (ps) time regime (Supplementary Fig. 2f). These data indicate a strong difference in the deactivation path for Ziapin2 in the two solvents, with a relatively fast emission lifetime in DMSO (8 ps), consistent with the photoisomerization reaction, and a marked slowdown of the lifetime in water (26 ps) due to the formation of molecular aggregates. Interestingly, in sodium dodecyl sulphate (SDS) we observed a 25% decrease of the lifetime when compared with water, an effect that can be attributed to the partially recovered isomerization ability of membrane-embedded Ziapin2. Aggregation was also investigated by UV–Vis and PL spectra as a function of concentration (Supplementary Fig. 3a–c) and on water addition (Supplementary Fig. 3d–f). While normalized absorption spectra of Ziapin2 show little dependence on concentration, PL exhibits a linear redshift, suggesting the occurrence of an excited state interaction. Absorption/PL spectra for Ziapin2 at fixed concentration (25 μM) and different DMSO/water ratios show a growing a redshift upon water addition alongside an increase of PL intensity (Supplementary Fig. 3d–f). The broad, featureless and Stokes-shifted emission suggests the formation of aggregates with an excimeric-like deactivation, similarly to that observed for confined azobenzene derivatives in nanostructured silica[30].

Interestingly, the PL spectra of Ziapin2 in SDS micelles, mimicking the bilayer environment[31], and in cell membranes essentially coincide, lying between DMSO and water spectra (Supplementary Fig. 2c). Total internal reflection fluorescence microscopy on model bilayers composed of either phosphatidylcholine (PC) or a mixture of PC, cholesterol and sphingomyelin (SM), mimicking the composition of lipid rafts, confirmed the spectral overlap among Ziapin2 PL in SDS micelles, model membranes and raft-like membranes (Supplementary Fig. 4). Similarly, the photoswitching dynamics in either SDS micelles (Supplementary Fig. 2d) or cell membranes (Fig. 1f) were intermediate between the fast photoswitching behaviour in DMSO and the frozen photodynamics observed in aqueous media. The non-exponential PL decay in the cell membrane (Fig. 1g) reflects the relaxation time distribution in disordered environments, such as lipid rafts or local phase/thickness changes. Although the molecular event of photoisomerization occurs in the sub-ps time scale, the sizable change observed in the time evolution of the isomeric populations in the ensemble is associated with a macroscopic fraction of isomerized molecules. All these findings suggest that the partition of the molecule in lipid membranes avoids the aggregation of Ziapin2, enabling effective isomerization and light-controlled photoswitching.

Ziapin2 increases membrane capacitance

We performed molecular dynamics (MD) simulations placing one molecule of Ziapin2 in *trans* conformation in the water region, parallel to a PC membrane and in different orientations. In three simulations, the molecule entered the bilayer within 100 ns and remained in the membrane for the rest of the trajectory (Fig. 2a,b). In all cases, Ziapin2 entered the membrane by first piercing it with the azobenzene side and then moving towards the centre of the bilayer by keeping the elongated axis almost parallel to the bilayer normal (Fig. 2a; I–IV). The insertion stopped when the positively charged pyridine rings were at the level of the lipid heads, coordinated by phosphate groups. Interestingly, in a different simulation, one Ziapin2 molecule placed at the centre of the bilayer and parallel to it reached very rapidly (<5 ns) the same equilibrium position. The insertion process was quantitatively studied by calculating the associated free-energy profile (Fig. 2c). We found essentially no barrier for Ziapin2 adsorption in the membrane, a pronounced minimum at the equilibrium position spontaneously obtained before and a barrier for membrane desorption to water of ~12 kcal mol^{-1} (0.52 eV).

Before studying the cellular distribution and effects of Ziapin2 in neurons, we demonstrated that Ziapin2 did not elicit any toxic or inflammatory reaction in neurons (Supplementary Figs. 5 and 6).

Next, primary hippocampal neurons loaded with Ziapin2 were live-stained with the plasma membrane reporter CellMask and subjected to three-dimensional confocal imaging (Fig. 2d). The quantification revealed that more than 70% of Ziapin2 was localized to the neuronal surface, with a coverage of ~15% of the total membrane surface (Fig. 2d–f) that progressively decreased over time ($t_{1/2} = 36.4$ h, Supplementary Fig. 7a). The occurrence of fluorescence resonance energy transfer between Ziapin2 and CellMask further demonstrates that Ziapin2 is strictly localized to the membrane bilayer (Supplementary Fig. 7b,c).

Given the punctate distribution of Ziapin2 fluorescence on the plasma membrane, we evaluated the colocalization of Ziapin2 with lipid rafts[32] by live labelling with cholera toxin β-subunit and high-resolution fluorescence microscopy with structured light (SIM; Fig. 2e). Interestingly, the percentage of Ziapin2 colocalizing with lipid rafts (~60%) was only slightly smaller than that observed with CellMask and covered a substantially higher proportion (~25%) of the total raft surface with respect to CellMask (Fig. 2e,f). To unambiguously demonstrate the propensity of Ziapin2 for lipid rafts, we treated primary neurons with methyl-β-cyclodextrin (MβCD) to partially deplete membrane cholesterol and decrease the density of lipid rafts (~50% decrease based on Filipin staining; Supplementary Fig. 8a; Fig. 2g). Strikingly, MβCD markedly altered the punctate distribution of Ziapin2 in the membrane by decreasing the density of Ziapin2-positive puncta and increasing the Ziapin2-positive
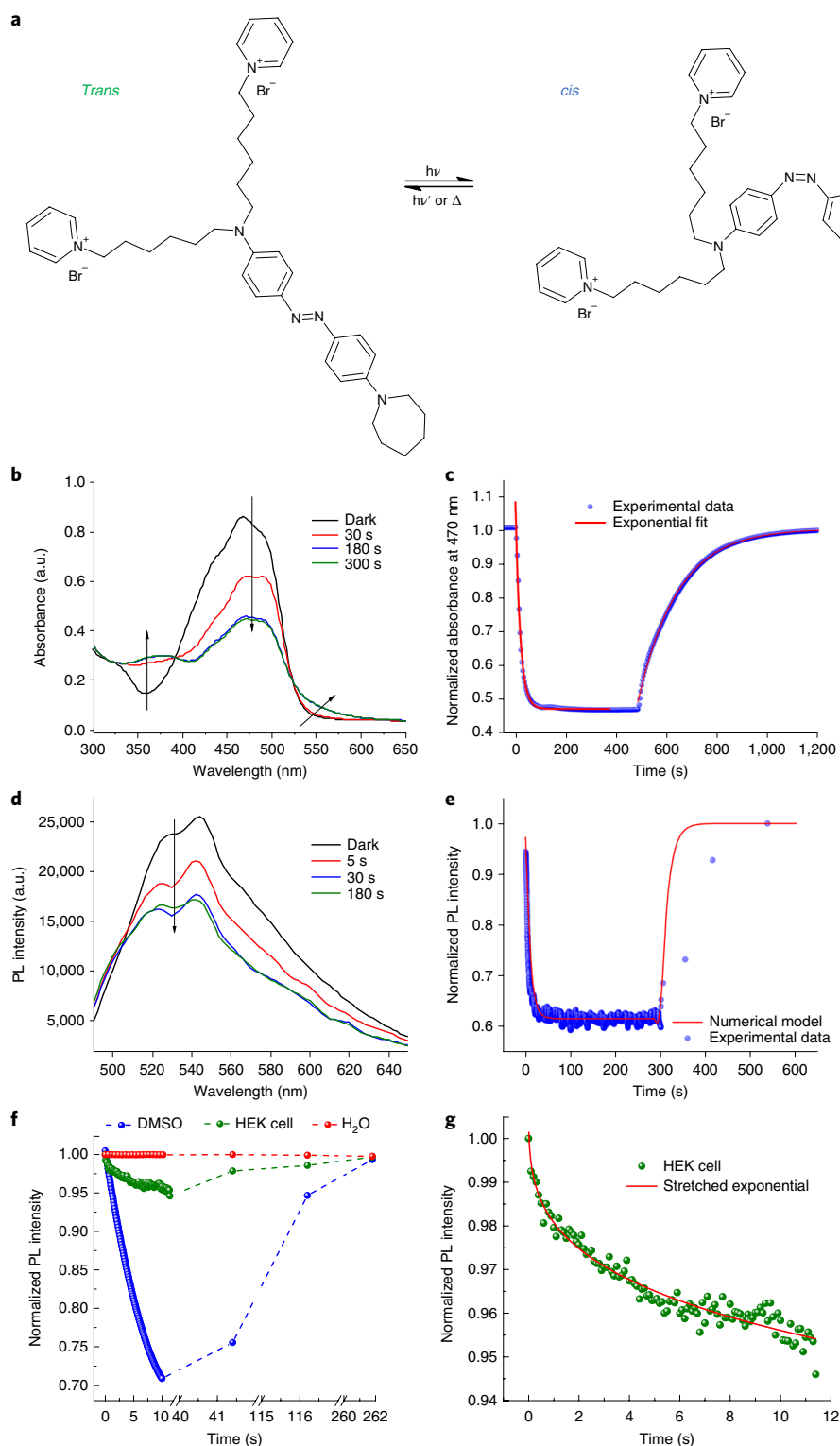
Fig. 1 | *Trans→cis* isomerization of Ziapin2 in various environments. a, Schematic of the isomerization process in Ziapin2. **b,c**, Changes in the Ziapin2 absorbance spectrum (25 μM in DMSO) as a function of time (**b**) and time course of absorbance at 450 nm upon illumination with a diode laser (**c**). The collective photoswitching dynamics upon light exposure reveals a well-defined and relatively fast photoreaction dynamics of Ziapin2 in DMSO, reaching a photostationary population after about 100 s of illumination and achieving a complete recovery with a $t_{1/2}$ of 108 s in the dark at room temperature. While the photoisomerization process occurs typically in the picosecond range, the population dynamics towards the photostationary state takes much longer, depending on the conformer thermodynamic stability and molecular environment. **d,e**, Changes in the Ziapin2 PL spectrum (25 μM in DMSO) as a function of time (**d**) and time course of the emission at 540 nm upon excitation at 450 nm with a Xenon lamp (**e**). The red line is the numerical model employed to describe the time evolution of the fluorescence signal. **f**, Photoswitching/relaxation dynamics of Ziapin2 in DMSO, human embryonic kidney 239 (Hek293) cells and water acquired by exciting at 450 nm and collecting the emission at 540, 580 and 620 nm, respectively. **g**, Zoom on the PL dynamics in Hek293 cells, highlighting the stretched exponential decay. Such function considers the distribution of relaxation times occurring in disordered environments. a.u., arbitrary units.

areas, indicative of release of the probe from the rafts and its dispersion within the membrane (Fig. 2g,h).

Spatially resolved membrane thickness maps calculated from simulations of multiple Ziapin2 molecules in *trans* or *cis* conformations revealed the presence of thinner bilayer regions in the *trans* case (Fig. 3a and Supplementary Fig. 9). Indeed, *trans* Ziapin2 molecules anchored to the opposite leaflets of the membrane form dimers via backbone interaction, pulling lipid heads towards the centre of the bilayer and resulting in a local depression of the membrane (Fig. 3a, left panels). Conversely, when Ziapin2 is in *cis* conformation, the hydrophobic tails of opposed molecules are too far from each other to dimerize, leaving the membrane thickness unperturbed (Fig. 3a, right panels). A similar bilayer depression, associated with *trans* Ziapin2 dimerization, was observed in a lipid raft model (Fig. 3b).

We then investigated by atomic force microscopy (AFM) whether insertion of Ziapin2 in artificial membranes affects bilayer thickness. According to MD predictions, incorporation of *trans* Ziapin2 in unilamellar liposomes composed of either PC or a raft-like mixture induced a significant reduction in membrane thickness that was more extended and pronounced in the raft-mimicking environment (Fig. 3c,d and Supplementary Fig. 10).

Given the inverse proportionality between capacitance and thickness, we measured the capacitance of stably preformed planar membranes of PC or raft-like composition after addition of *trans* Ziapin2 to one or both sides of the bilayer. Unilateral addition of Ziapin2 increased the bilayer capacitance in both types of membrane, an effect that became significantly larger when Ziapin2 was added on both sides (Fig. 3e and Supplementary Fig. 11a).

We then checked whether Ziapin2 in the dark had any effect on capacitance in a simple cell model (Hek293; Fig. 3f). The addition of Ziapin2 induced a significant increase in capacitance ($32.1 \pm 1.7\,pF$), probably attributable to the bilayer thinning caused by Ziapin2 *trans*-dimerization, while the DMSO vehicle was ineffective ($26.4 \pm 1.4\,pF$; see Supplementary Materials and Supplementary Fig. 11b–d).

Light-induced neuronal activity by Ziapin2 in vitro

MD simulations predict that light-induced *trans*→*cis* photoconversion of Ziapin2 would relax the membrane towards its native thickness (Supplementary Fig. 12), thereby reversing the effect on membrane capacitance. When light stimuli were administered to Ziapin2-loaded Hek293 cells, the increased capacitance returned towards basal levels (mean decrease $\pm$ s.e.m.: $4.4 \pm 0.5\,pF$) while vehicle-loaded cells did not respond to light (Supplementary Fig. 13a; cf. Fig. 3f). Such effect was associated with membrane hyperpolarization, peaking ~13 ms after light onset and followed by a delayed depolarization (Supplementary Fig. 13b,c), as reproduced by a numerical simulation of the membrane equivalent circuit (Supplementary Fig. 13d). We next tested the physiological effects of Ziapin2 in primary hippocampal neurons (Fig. 4a). In the dark, a significant capacitance increase was observed (from $32.4 \pm 1.7\,pF$ to $53.3 \pm 6.0\,pF$; Fig. 4b), without significant changes in other passive membrane properties (Supplementary Figs. 11e–g and 14a). When Ziapin2-loaded neurons were photostimulated, a fast and significant capacitance drop (mean decrease $\pm$ s.e.m.: $6.5 \pm 1.1\,pF$) was observed, followed by a slow return to the pre-illumination level (Fig. 4b). The change in capacitance peaked a few ms after light onset and was not significantly different between 20 and 200 ms of light stimulation. Notably, a significant correlation was observed between the *trans* Ziapin2 capacitance increase and the light-induced capacitance drop (Fig. 4b).

Ziapin2-labelled neurons showed a biphasic modulation of the membrane potential characterized by an early hyperpolarization, with a time course overlapping with the capacitance change, followed by a delayed depolarization of similar amplitude (Fig. 4c,d). While the hyperpolarization peak occurred with similar latency with 20 or 200 ms, the peak depolarization was delayed with 200 ms stimuli (Fig. 4e). To distinguish intrinsic effects from the effects of the reverberant network of synaptic connections, we employed blockers of excitatory and inhibitory synaptic transmission. Under these conditions, the magnitude and timing of hyperpolarization were unaffected (Fig. 4c,d; $P = 0.79$ and $P = 0.69$, Mann–Whitney U test), while the amplitude of the depolarization was significantly decreased (Fig. 4c,d; $P < 0.01$ for both 20 and 200 ms stimuli, Mann–Whitney U test), similarly to that observed in Hek293 cells (Supplementary Fig. 13b,c). These data indicate that light-induced hyperpolarization is an intrinsic effect resulting from the drop in capacitance, while the late depolarization response of neurons is amplified by the network synaptic transmission.

We then ran voltage-clamp experiments in Ziapin2-loaded neurons to build I/V plots of the light-induced transient capacitive current. Light stimulation (20 ms) elicited outward and inward currents at negative and positive potentials, respectively, with an inversion at approximately 0 mV, as expected by a pure capacitive current.

Fig. 2 | Ziapin2 distributes to the plasma membrane and lipid rafts in neurons. a, Snapshots extracted from an MD simulation showing Ziapin2 (*trans*) spontaneously entering the membrane (PC lipid model) at consecutive time frames (I–IV); lipid phosphate atoms are shown as orange spheres and acyl chains as grey lines; water molecules are not reported for clarity. **b**, Time dependence of the distance between the centre of mass (COM) of Ziapin2 and the bilayer centre in three independent simulations; the dashed line indicates the interface between water and lipid head groups. **c**, Free-energy profile for Ziapin2 (*trans*) entering the membrane bilayer, calculated versus the distance between the bilayer centre and the centre of mass of the two pyridinic nitrogens of Ziapin2. **d**, Primary neurons pulse exposed to Ziapin2 for 7 min were stained with the specific plasma membrane reporter CellMask (red) to evaluate the membrane incorporation of Ziapin2 (green). Scale bars: 10 and 20 μm for large and small panels, respectively. **e**, Primary neurons pulse exposed to Ziapin2 (green) for 7 min were stained with the specific lipid raft marker Vybrant Alexa Fluor 555 (red) with or without pretreatment with methyl-β-cyclodextrin (MβCD) to deplete cholesterol and imaged by structured illumination microscopy (SIM). Scale bars: 5 and 2 μm for large and small panels, respectively. **f**, Analysis of z-stack confocal images of CellMask/Ziapin2 and Vybrant/Ziapin2 double-stained neurons. Upper panel: Partitioning of Ziapin2 to the plasma membrane and lipid rafts was evaluated as the percentage of total cell Ziapin2 fluorescence colocalizing with the respective marker 7 min after loading and subsequent washout. Means $\pm$ standard error of the mean (s.e.m.) with individual experimental points are shown. Lower panel: Percentage of the total plasma membrane (CellMask staining) or lipid raft domains (Vybrant staining) that were positive for Ziapin2 7 min after loading. Means $\pm$ s.e.m. with individual experimental points are shown. The Vibrant/CellMask surface ratio, determined in parallel samples double labelled with the two probes, was $71 \pm 2\%$. ***$P < 0.001$, unpaired Student's t test ($n = 26$ and 39 for CellMask and Vybrant staining, respectively, from three independent primary neuronal preparations). **g**, Effects of cholesterol depletion on the membrane distribution of Ziapin2. Representative images of Ziapin2 clusters acquired by SIM imaging in control neurons and neurons pretreated with MβCD. Scale bars: 2 μm. The line-scan fluorescence intensity plots reveal a dot-pattern profile for untreated (Ctrl) samples (black traces) and a more diffuse signal for MβCD-treated cells (red traces). **h**, The density of Ziapin2 clusters and of Vybrant-labelled rafts (puncta μm^{-2}) and their average size were evaluated washout in Ctrl and MβCD-treated neurons after 7 min of Ziapin2 labelling and subsequent live staining with Vybrant to label lipid rafts. Means $\pm$ s.e.m. with individual experimental points are shown. **$P < 0.01$; ***$P < 0.001$, Kruskal-Wallis/Dunn's test ($n = 20$ for Ctrl and MβCD, respectively, from three independent neuronal preparations).

Consistently, no changes were observed in the I/V plots when choline replaced extracellular Na⁺ or a cocktail of ion channel blockers for passive and active conductances was used (Supplementary Fig. 15a,b and Methods). These treatments also left unaltered

the hyperpolarization response to light when the recording was switched to current-clamp (Supplementary Fig. 15c,d).

The hyperpolarization response to light of neurons that had been partially depleted of membrane cholesterol by MβCD (see
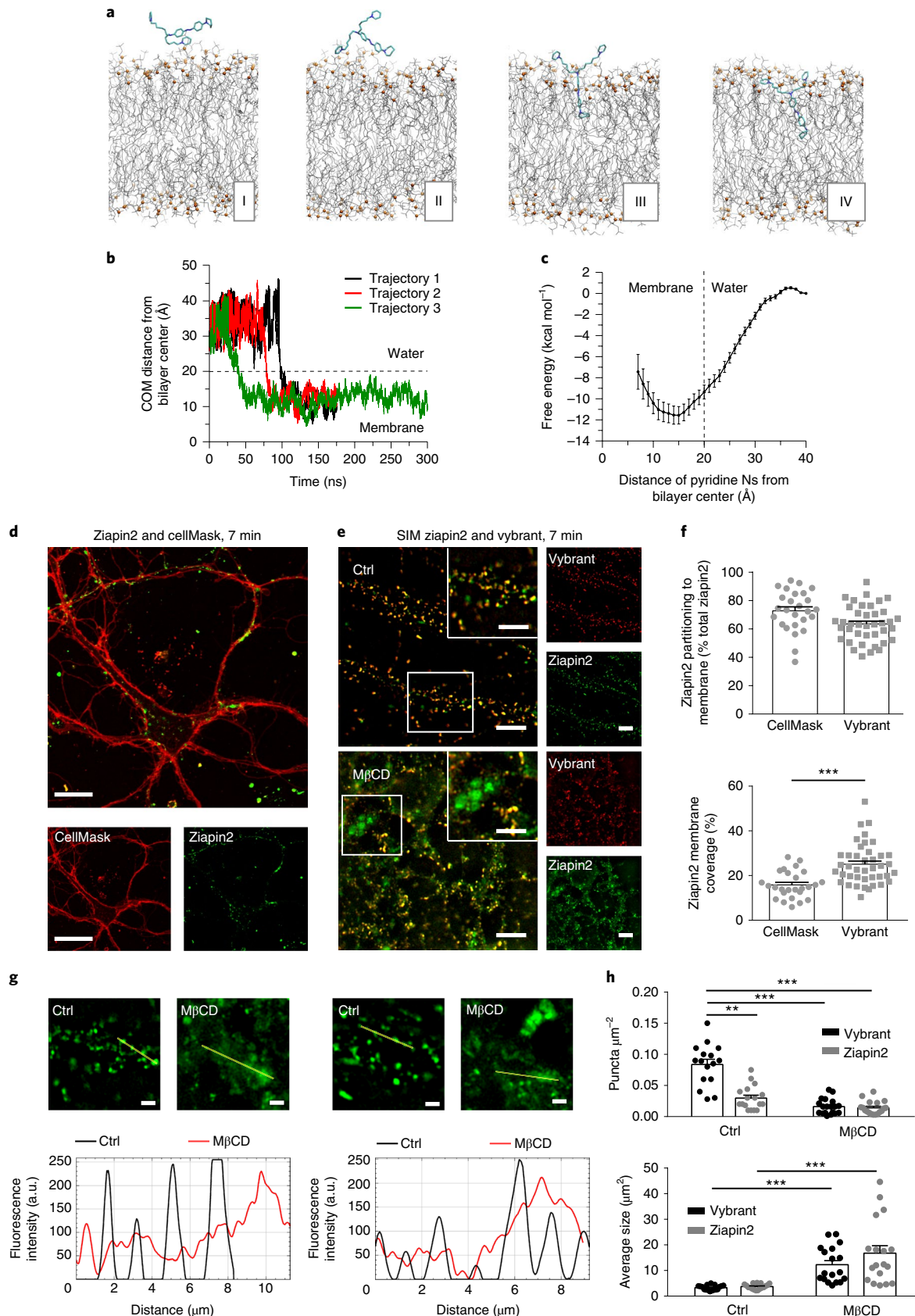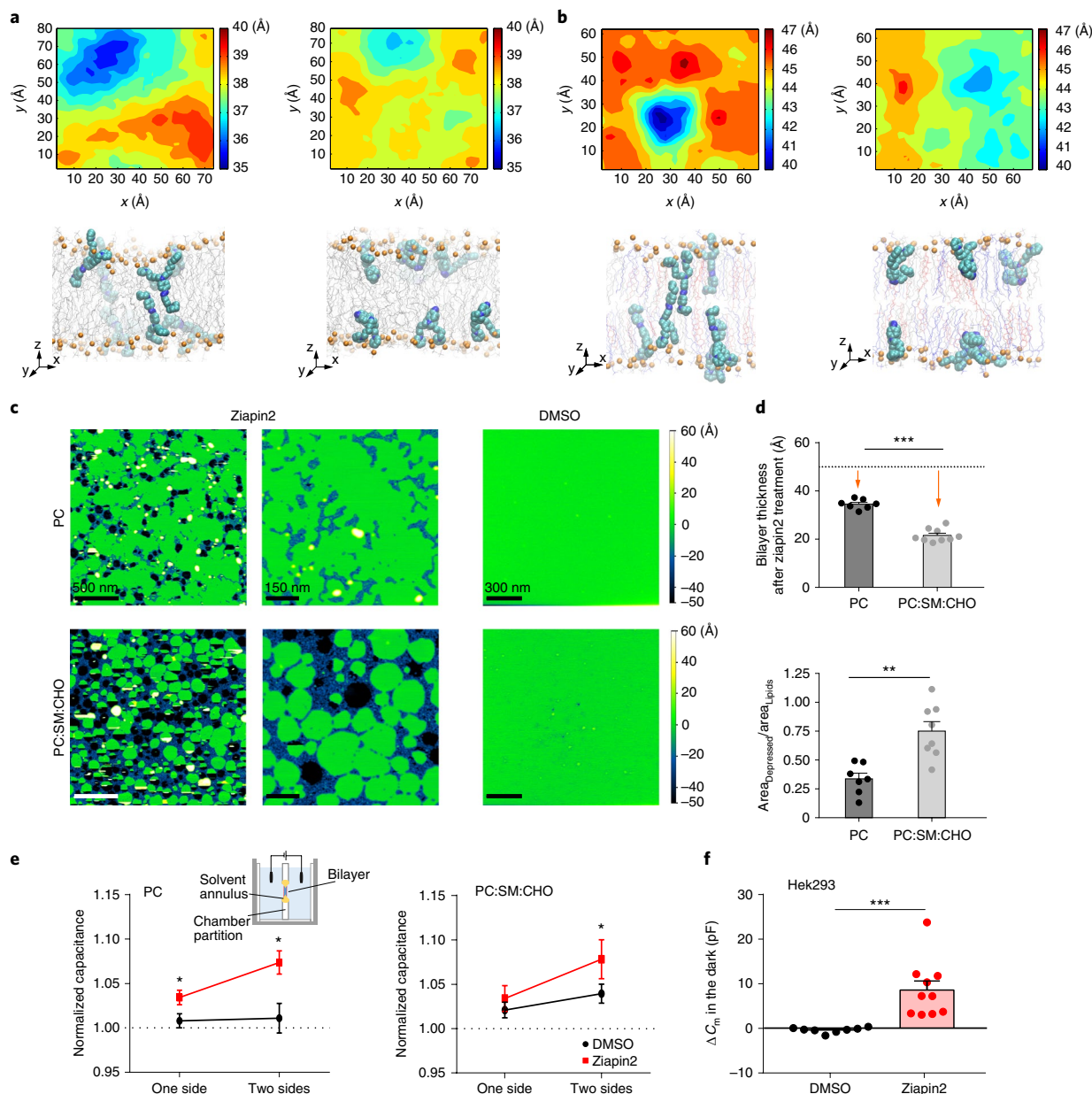
Fig. 3 | Ziapin2 reversibly modifies membrane thickness in artificial membranes, cell lines and neurons. a, Upper panels: Average membrane thickness maps, shown perpendicular to the bilayer plane, for the simulations of Ziapin2 (eight molecules) in *trans* (left) and *cis* (right) conformations, respectively. Ziapin2 molecules were embedded in PC model membranes. For the two Ziapin2 conformations, simulations (200 ns trajectory⁻¹) were started with the molecule in the equilibrium position. In both cases, the position along the bilayer normal was stationary over the whole trajectory, while the orientation fluctuated between a parallel and a perpendicular state. Axis and thickness values are in Å. Lower panels: Snapshots from simulations of Ziapin2 (eight molecules) in *trans* (left) and *cis* (right) conformations, respectively. **b**, Upper panels: Average thickness maps of a raft membrane model (simulations with eight Ziapin2 molecules in *trans* (left) and *cis* (right) conformations, respectively). The raft membrane model is composed of a mixture of PC, SM and cholesterol (CHO) (1:1:1). Axis and thickness values are in Å. Lower panels: Snapshots from the simulations of eight Ziapin2 molecules in *trans* (left) and *cis* (right) conformations. PC lipid molecules are shown as grey lines, and phosphate atoms as orange spheres; cholesterol and SM molecules are shown as red and blue lines, respectively; water molecules and ions are not reported for clarity. **c**, AFM maps realized in liquid environment on lipid bilayers formed either by PC (top) or by PC:SM:CHO (bottom) on mica and exposed to Ziapin2 or DMSO. Maps of Ziapin2-containing bilayers show the spatial distribution of depressed areas and the fine structure of the roughness modulation (left and middle panels at different magnification), while DMSO-containing bilayers show a very well-preserved uniformity (right). **d**, Top: Bilayer thickness after Ziapin2 incorporation in the dark with respect to the untreated nominal value (broken line). Bottom: Ratio between the area of depressed membrane and the total lipid-covered area. Raft-like bilayers show a higher decrease in thickness (top) and a more extended area of depression (bottom) when exposed to Ziapin2 if compared with single PC bilayers. The effects of Ziapin2 on thickness and depressed area are statistically significant for both types of bilayer ($P < 0.05$ for both PC and PC:SM:CHO, one sample Student *t* test) and significantly more pronounced in raft-like than in pure PC membranes (***$P < 0.001$, Mann–Whitney *U* test, $n = 7$ and 9 for PC and PC:SM:CHO, respectively). **e**, Planar lipid membrane experiments realized with PC (left) or PC:SM:CHO (right) show a systematic increase of capacitance measured across the bilayers when Ziapin2 was present in both recording chambers with respect to the sole insertion in one of the two sides. *$P < 0.05$, Mann–Whitney *U* test ($n = 6$ and 5 for Ziapin2 and DMSO, respectively, for each type of bilayer). **f**, Evaluation of cell capacitance changes (means ± s.e.m.) by patch-clamp recordings after exposure of Hek293 cells to either DMSO (0.25% v/v; black) or Ziapin2 (5 μM in DMSO; red) in the dark. °°°$P < 0.001$, Mann–Whitney *U* test ($n = 8$ and 9 for DMSO and Ziapin2, respectively).
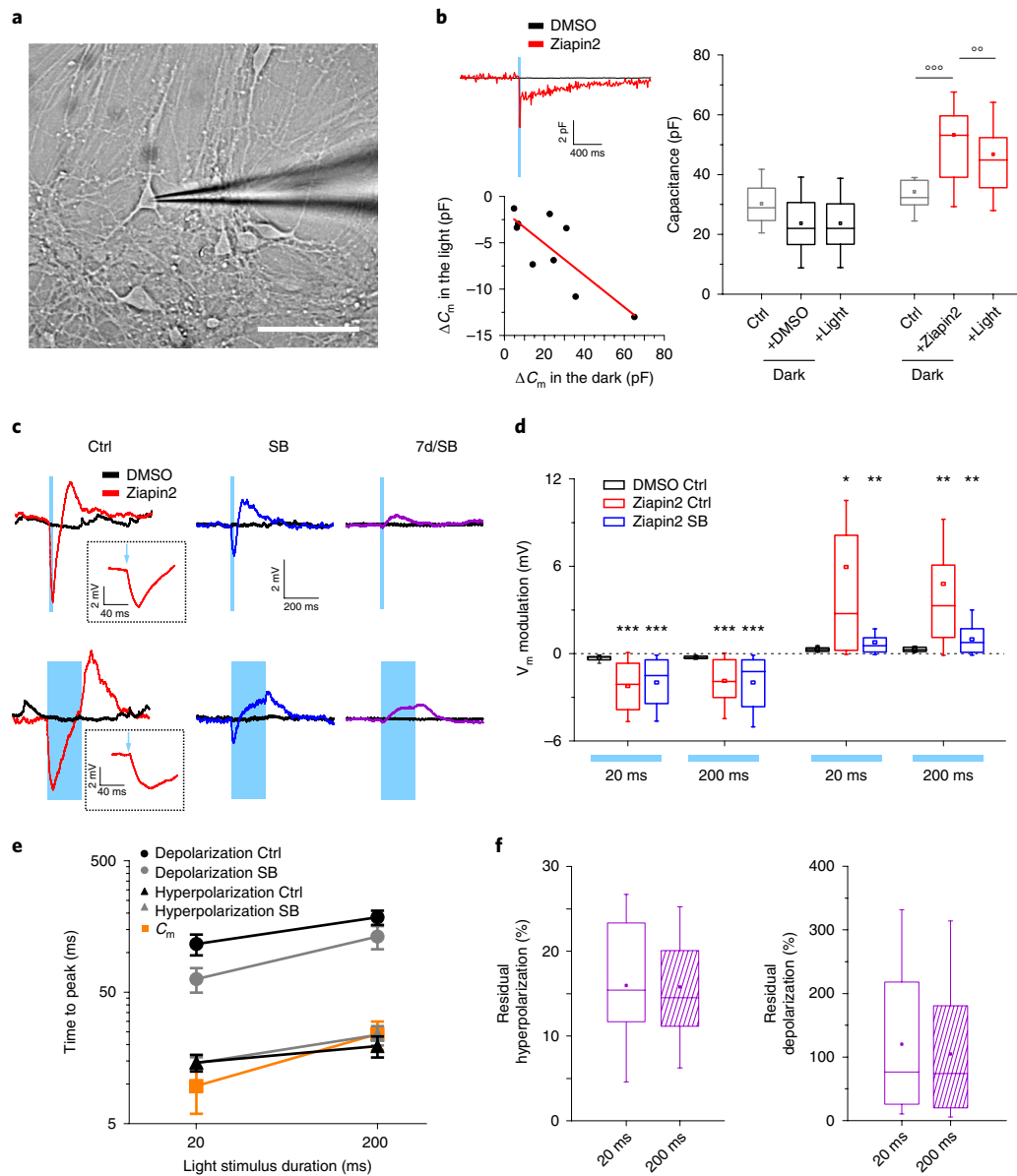
Fig. 4 | Light-evoked membrane voltage modulation by Ziapin2 in primary neurons. a, Primary hippocampal neurons at 14 days in vitro were incubated with Ziapin2 for 7 min, washed and recorded by whole-cell patch-clamp either immediately after pulse labelling or 7 d after. Scale bar: 20 μm. **b**, Left: Representative averaged capacitance traces of neurons pulse labelled with either DMSO (0.25% v/v; black traces) or Ziapin2 (5 μM in DMSO; red traces), washed and recorded in current-clamp configuration in the presence of SB before and after light stimulation (470 nm; 18 mW mm^{-2}; cyan-shaded areas). In the bottom panel, single-cell correlation between the capacitance increase in the dark upon Ziapin2 addition (x axis) and the phasic capacitance drop induced by light (y axis). Pearson's correlation coefficient −0.801, $P < 0.05$. Right: Box plots of the peak capacitance changes after exposure of neurons to either DMSO (0.25% v/v; black) or Ziapin2 (5 μM in DMSO; red) in the dark (DMSO, $n = 11$; Ziapin2, $n = 13$) and subsequent illumination in the presence of the compound and of SB. The same neurons were recorded under basal conditions, added with either DMSO or Ziapin2 and finally stimulated with light. $**P < 0.01$; $***P < 0.001$; Ziapin2 versus DMSO, Friedman/Dunn's tests. **c**, Representative whole-cell current-clamp traces recorded from neurons incubated with either 0.25% (v/v) DMSO (black traces) or 5 μM Ziapin2 in DMSO (red traces) in the absence (Ctrl) or presence of SB (Methods) and after 7 d of incubation in the presence of SB (7d/SB). The duration of the light stimulation (20 and 200 ms) is shown as a cyan-shaded area (470 nm; 18 mW mm^{-2}). In the insets, traces are shown in an expanded timescale. **d**, Box plots of the peak hyperpolarization (left) and peak depolarization (right) changes in primary neurons exposed to DMSO/Ziapin2 and subjected to 20/200 ms light stimulation in the absence (Ctrl) or presence of SB. Hyperpolarization and depolarization were measured as the minimum and maximum voltage, respectively, reached within 350 ms from light onset. The box plots show that the peak hyperpolarization response generated by the presence of Ziapin2 is an intrinsic response of the neuron and is not affected by the presence of blockers of synaptic transmission, while depolarization, already present in synaptically isolated neurons, is enhanced by active synaptic transmission. **e**, Time-to-peak hyperpolarization, depolarization and capacitance changes as a function of the light stimulus duration under Ctrl and synaptic block conditions. Data (means ± s.e.m.) represent the time necessary to reach the minimum and maximum membrane voltages in the above-mentioned time windows. **f**, Persistence of the light response over time. The residual light-induced hyperpolarization (left) and depolarization (right) effects observed 7 d after the initial Ziapin2 loading in the presence of SB are expressed in percentage of the corresponding effects measured acutely after Ziapin2 loading. Box plots are shown for both 20 and 200 ms light stimuli. All experiments with neurons were carried out at 24 ± 1 °C. $*P < 0.05$; $**P < 0.01$; $***P < 0.001$ DMSO versus Ziapin2, Mann–Whitney U test. Ziapin2-treated neurons: $n = 19, 20, 15$ (20 ms) and $n = 20, 19, 14$ (200 ms) for Ctrl, SB and 7d/SB, respectively; DMSO-treated neurons: Ctrl, SB, 7d/SB: $n = 10, 7, 10$ for both 20 and 200 ms.
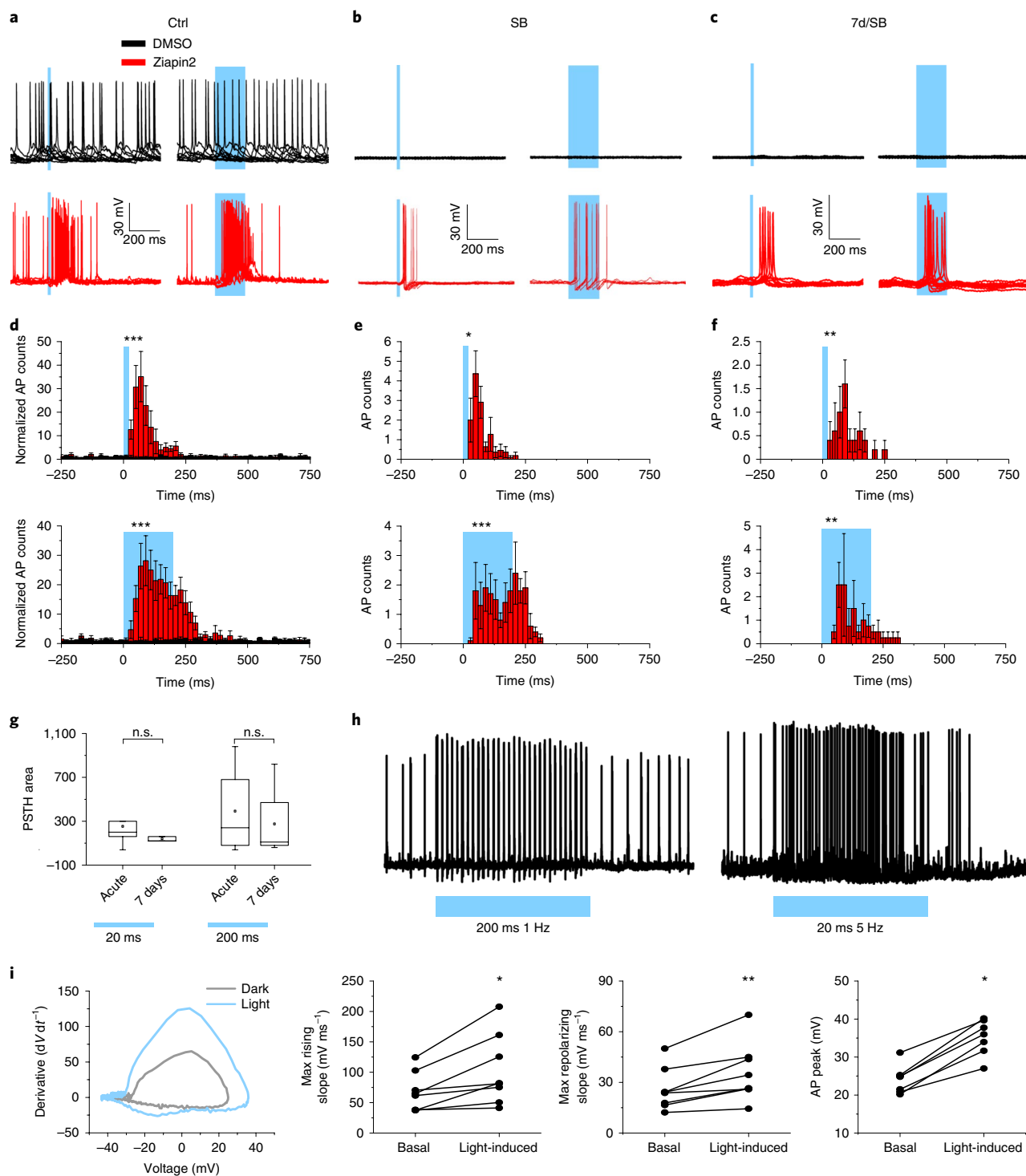
Fig. 5 | Light-evoked firing activity in primary neurons loaded with Ziapin2. a–c, Representative averaged traces recorded in current-clamp configuration from neurons incubated with either DMSO (0.25% v/v, black traces) or Ziapin2 (5 µM in DMSO, red traces) in the absence (**a**; Ctrl) or presence (**b**) of SB. In **c**, recordings were performed 7 d after Ziapin2 labelling with SB. Light stimulation (470 nm; 18 mW mm^{-2}) is shown as a cyan-shaded area. **d–f**, Peristimulus time histograms (PSTHs) (bin = 20 ms) reconstructed from the firing rate of neurons recorded in the absence (**d**) or presence of SB 7 min (**e**) and 7 d (**f**) after DMSO/Ziapin2 labelling, respectively, and subjected to either 20 ms (upper panel) or 200 ms (lower panel) light stimulation. Ziapin2-treated neurons: n = 7, 11, 5 (20 ms) and n = 6, 10, 4 (200 ms) for Ctrl, SB, 7d/SB, respectively; DMSO-treated neurons: n = 4, 7, 10 (20 and 200 ms) for Ctrl, SB, 7d/SB, respectively. *P < 0.05; **P < 0.01; ***P < 0.001 DMSO versus Ziapin2, Mann–Whitney U test on 160 ms bins (20 ms stimulation) and 240 ms bins (200 ms stimulation). **g**, PSTH areas of AP firing in response to 20/200 ms light stimulation in the presence of SB recorded either acutely or 7 d after Ziapin2 exposure. N = 10 (acute); N = 5 (7 d); n.s., not significant, Mann–Whitney U test. **h**, Representative AP firing activities recorded from neurons incubated with Ziapin2 (5 µM) in the absence of SB and stimulated with 200 ms light pulses administered at 1 Hz (upper traces) or with 20 ms light pulses administered at 5 Hz (lower traces). **i**, Left: Representative phase plane plot analysis of AP waveforms generated in the same Ziapin2-loaded neuron before (grey trace) and after (blue trace) light stimulation (470 nm; 20 ms pulses @ 20 mW mm^{-2}). Right: Quantification of the maximal rising and repolarizing slopes and of the AP peak amplitude before and after illumination. *P < 0.05; **P < 0.01, paired Student's t test (n = 7 neurons).

above; Supplementary Fig. 8a,b) was then investigated. Cholesterol depletion reduced the amplitude of light-evoked hyperpolarization in Ziapin2-labelled neurons, suggesting that clustering of Ziapin2 molecules at cholesterol-enriched membrane domains is essential for enhancing the light-dependent effects on membrane thickness (Supplementary Fig. 8b,c).

Morphological studies indicated that ~30% of the initial Ziapin2 labelling was present on the plasma membrane 7 d after loading, with a parallel reduction of light-evoked hyperpolarization with respect to acute Ziapin2 (Fig. 4f and Supplementary Fig. 7). However, the delayed depolarization was only slightly decreased (Fig. 4f), suggesting that the reduced membrane Ziapin2 concentration decreases the extent of light-evoked capacitance drop, leaving the return to basal capacitance relatively unaffected.

The steady increase in membrane capacitance induced by Ziapin2 in the dark significantly increased the rheobase and slowed AP's spontaneous frequency. Analysis of the AP waveform by phase plane plot revealed a slowdown of the rising and repolarizing slopes and an increased AP half-width in the absence of changes in AP amplitude (Supplementary Fig. 14b,c). We then examined the ability of light stimulation to elicit APs in Ziapin2-loaded neurons acutely and 7 d after membrane labelling (Fig. 5a–c). Light stimulation elicited a significant increase of AP frequency (Fig. 5a). Such result was even more striking in the presence of synaptic blockers (SB) that abolished spontaneous light-independent firing (Fig. 5b). Light-evoked firing was persistent over time, as shown 7 d after Ziapin2 labelling in the presence of SB (Fig. 5c). Peristimulus time histogram analysis showed that light reliably induced AP firing activity. AP firing peaked after light offset for short stimuli and during the light phase for long stimuli (Fig. 5d–g). Interestingly, repetitive firing was obtained with light pulse trains of 200 ms at 1 Hz or 20 ms at 5 Hz, with only occasional failures (Fig. 5h). Phase plane plot analysis of AP waveforms (Fig. 5i) revealed that light-evoked APs were characterized by increased rising/repolarization slopes and peak amplitudes, consistent with the light-induced drop in membrane capacitance.

Comparable light-evoked physiological effects of Ziapin2 described in murine neurons were also observed in human neurons differentiated from induced pluripotent stem cell (iPSC) clones generated from skin fibroblasts of healthy volunteers (Supplementary Fig. 16 and ref. [33]). We also compared the Ziapin2 effects with the photostimulation of primary neurons transduced with the ultra-fast microbial opsin ChETA, a light-dependent cationic channel[34] (Supplementary Fig. 17). As expected from a light-gated ion channel, ChETA induced a larger V_m modulation than Ziapin2 at all stimulus durations, although the peak-to-peak difference reached significance only in the presence of SB (Supplementary Fig. 17a). Notably, no significant differences were observed in the latency to the peak V_m change in the absence of APs (Supplementary Fig. 17a), as well as in the light-induced firing probability measured both at the resting membrane potential (-53.6 ± 0.9 mV) and with neurons depolarized near threshold (-35 mV; Supplementary Fig. 17c). However, ChETA was faster in the latency to the first light-induced AP (Supplementary Fig. 17d). Waveform analysis of light-evoked APs failed to detect differences between ChETA- and Ziapin2-labelled neurons, indicating that the light-induced decrease in capacitance in Ziapin2-loaded neurons normalized the AP dynamics (Supplementary Fig. 17e).

Light-induced cortical activity by Ziapin2 in vivo

Ziapin2 or vehicle was injected in the somatosensory cortex of mice subsequently implanted with a multielectrode array coupled with an optical fibre (Fig. 6a). Cortical responses to light stimuli were measured shortly after surgery (30–60 min) and 1, 4 and 7 d after the Ziapin2 injection. Ziapin2 fluorescence analysed in brain slices showed a diffusion diameter in the range of 1 mm and persisted up to 7 d from injection (Fig. 6b). Immunohistochemistry in cortical slices at the injection site performed 7 d after the injection demon-

strated that Ziapin2 did not alter the inflammatory reaction to the surgery, as evaluated by the expression of GFAP and Iba1, specific markers for astrocytes and microglia, respectively (Supplementary Fig. 18). Optical stimulation at various power densities induced activation of cortical activity evaluated as extracellular local field potentials (LFPs) that peaked at about 200 ms after light onset (Fig. 6c). Ziapin2 induced a significant dose-dependent increase in the LFP amplitude with respect to vehicle-injected animals that was more pronounced for 200 ms stimuli (Fig. 6d). Analysis of the time course of the light-evoked LFP responses revealed that the optical stimulation of cortical activity persisted up to 7 d after injection (Fig. 6e,f).

Conclusions

We report here on an opto-mechanical effect driven by intramembrane molecular machines composed of clustered photochromic molecules. The predictions by MD simulations, confirmed by experimental observations on artificial membranes, are consistent with a model in which the hydrophobic azepane-substituted aniline in the amphiphilic azobenzenes on the two sides of the membrane interact when in *trans* configuration, retracting to *cis* after photoconversion. This brings about shrinkage of the membrane on *trans* Ziapin2 loading that eventually relaxes to the natural thickness following light-induced Ziapin2 dissociation. The evoked relaxation increases membrane thickness, thus transiently decreasing its capacitance.

Ziapin2 differentiates from previously reported capacitance-changing azobenzene-cored amphiphilic probes containing long alkyl chains[6–8,35,36] for distinctive functional groups and features: (1) the two hexyl chains ω-terminated with pyridinium bromide that target the membrane;[35,36] (2) the presence of an amine on both azobenzene sides that, as strong electron-donor group, redshifts azobenzene absorption to the visible; (3) the azepane moiety that mediates the formation of *trans*-Ziapin2 dimers through the interaction between two facing Ziapin2 molecules on opposite bilayer leaflets. Thanks to these features, Ziapin2 responds to millisecond-range visible light stimuli by deforming the membrane and causing the fast physiological effects.

The light-induced capacitance drop generates a pure capacitive current responsible for a hyperpolarizing shift that depends on membrane coverage and rate of capacitance change. These effects do not involve ion channels, being recapitulated by Hek293 cells and neurons subjected to intra/extracellular blockade of membrane conductances. Thus, we are exploiting a novel membrane nanomachine with a mechanical effect at the molecular scale.

Although the existence of lipid rafts is a matter of controversy[37], photochromic molecules have already been targeted to lipid rafts[38]. The propensity of Ziapin2 to localize to cholesterol and sphingolipid-enriched membrane microdomains is functionally important. Indeed, the membrane-thinning effect, evaluated by AFM, was amplified in raft-like bilayers, and disruption of lipid rafts caused disappearance of Ziapin2 clusters and decrease of light-induced hyperpolarization.

Several papers reported a link between temperature-dependent decrease in membrane thickness, increased capacitance and depolarization[22–25], demonstrating that membrane capacitance is effective in modulating neuronal activity. In the dark, Ziapin2-induced increase in capacitance renders neurons less excitable and more refractory to membrane-voltage changes. This stabilization of neuronal activity is a potentially exploitable effect in the regulation of network excitability and in demarcating the discharge areas in neuronal networks. In response to light stimulation, Ziapin2 controls AP firing through two cooperating mechanisms: (1) the fast light-induced C_m decrease, generating hyperpolarization, followed by a slower C_m increase at the light offset, associated with rebound depolarization, as predicted by the equivalent circuit simulation; (2) membrane hyperpolarization may cause an 'anode break excita-
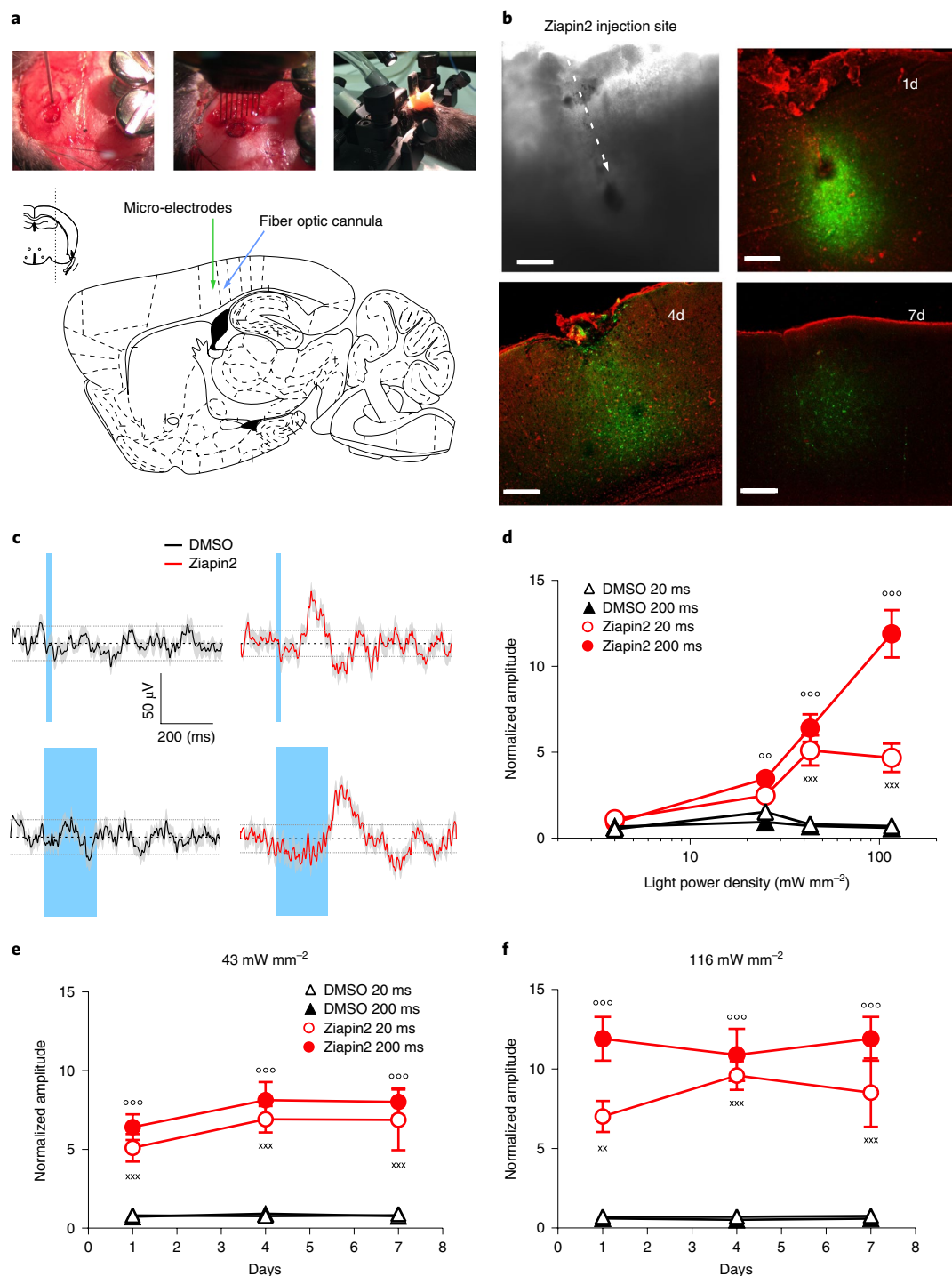
Fig. 6 | Light-evoked cortical responses in vivo in mice loaded with Ziapin2 in the somatosensory cortex. a, Schematic representation of the stereotaxic injection of Ziapin2 (200 μM in 1 μl 10% DMSO) in the somatosensory cortex (S1ShNc, 2 mm anterior to lambda, 2 mm lateral to midline, and −723 μm ventral to brain surface) and of the 16-microelectrode array implant for LFP recordings coupled with optical fibre for photostimulation. **b**, Bright field image (left) and endogenous LC339 fluorescence micrograph (right) of unfixed slices from the injected somatosensory cortex taken 1, 4 and 7 d after Ziapin2 administration. The injection site and the diffusion of the compound are visible. Scale bar: 150 μm. **c**, Representative recordings of LFPs evoked in the somatosensory cortex by 20 and 200 ms light stimulation (43 mW mm^{-2}) in mice injected with either DMSO (black trace) or Ziapin2 (red trace) 1 day before. The cyan-shaded areas represent the light stimulation. Potentials were considered significant above twofold the standard deviation range (broken horizontal lines). **d**, Dose-response analysis of LFP responses in DMSO- (black) or Ziapin2- (red) injected mice as a function of power and duration of the light stimulus (20 and 200 ms; open and closed symbols, respectively). The peak amplitude of light-evoked LFPs was normalized by the averaged noise amplitude calculated from the non-responding channels over the same epoch. Photostimulation at increasing power from 4 to 116 mW mm^{-2} triggered significant responses in Ziapin2-injected animals that were already significant at 25 mW mm^{-2} (200 ms stimulus). No significant responses were recorded in DMSO-treated animals. **e,f**, Time course of the normalized LFP amplitude recorded in the somatosensory cortex 1, 4 and 7 d after intracortical injection of either DMSO (black) or Ziapin2 (red). LFPs were evoked by 20 (open symbols) and 200 (closed symbols) ms light stimuli at 43 (**e**) and 116 (**f**) mW mm^{-2}. 20 ms: $^{xx}P < 0.01$, $^{xxx}P < 0.001$; 200 ms: $^{\circ\circ}P < 0.01$; $^{\circ\circ\circ}P < 0.001$; repeated measure ANOVA/Tuckey's tests versus DMSO-injected control ($n = 3$ mice for each experimental group).

tion' at the light offset, decreasing outward K$^+$ current and removing Na$^+$ channel inactivation[39]. The rebound post-hyperpolarization AP firing depends on the duration of membrane hyperpolarization[40], explaining the limitation in the maximal stimulation frequency that can be achieved.

Neurons display larger depolarization, with respect to Hek293 cells, that is sensitive to synaptic transmission, which instead does not affect hyperpolarization. Depolarization may contribute to the light-evoked firing through a positive feedback within the network mediated by excitatory synaptic transmission. In this respect, using conjugated polymer interfaces, we previously showed that light-induced inhibition is followed by a rebound depolarization and firing[19,23], indicating that the fast return of capacitance and voltage to basal levels is responsible for neuronal activation.

With respect to optogenetic light-gated ion channels such as ChETA, Ziapin2 does not interfere with ionic fluxes or reversal potential of membrane conductances but directly targets passive membrane properties. Although the Ziapin2 effect is slower than that of a light-driven ion channel, it has a comparable ability in eliciting of APs.

Ziapin2 is not harmful to primary neurons, and neuronal activation by Ziapin2 is persistent in vitro despite the slow decrease of the plasma membrane concentration due to membrane turnover. Moreover, Ziapin2 is effective in inducing a light-dependent electrical activation of the cortical networks after in vivo injection in the somatosensory cortex of the mouse, with a sustained effect of photostimulation and a complete absence of inflammatory responses to the compound, paving the way to their potential future in vivo applications.

In conclusion, our new amphiphilic photochromic molecules have several characteristics that differentiate them from previous compounds: (1) marked affinity for the hydrophobic environment of the membrane; (2) high tolerability and sensitivity to the visible spectrum; (3) reversible photoinduction of local membrane deformations altering membrane capacitance, potential and firing in the absence of heat generation; (4) effectiveness and prolonged effects in vivo. In view of these features, these molecules display a high potential for future applications in neurosciences and biomedicine.

Online content

Any methods, additional references, Nature Research reporting summaries, source data, extended data, supplementary information, acknowledgements, peer review information; details of author contributions and competing interests; and statements of data and code availability are available at https://doi.org/10.1038/s41565-019-0632-6.

References

1. Paoletti, P., Ellis-Davies, G. C. R. & Mourot, A. Optical control of neuronal ion channels and receptors. *Nat. Rev. Neurosci.* **20**, 514–532 (2019).
2. Rivnay, J., Wang, H., Fenno, L., Deisseroth, K. & Malliaras, G. Next-generation probes, particles, and proteins for neural interfacing. *Sci. Adv.* **3**, e1601649 (2017).
3. Tønnesen, J. Optogenetic cell control in experimental models of neurological disorders. *Behav. Brain Res.* **255**, 35–43 (2013).
4. Deisseroth, K. Optogenetics: 10 years of microbial opsins in neuroscience. *Nat. Neurosci.* **18**, 1213–1225 (2015).
5. Zhang, J. J., Wang, J. X. & Tia, H. Taking orders from light: progress in photochromic bio-materials. *Mater. Horiz.* **1**, 169–184 (2014).
6. Fujiwara, H. & Yonezawa, Y. Photoelectric response of a black lipid membrane containing an amphiphilic azobenzene derivative. *Nature* **351**, 724–726 (1991).
7. Yonezawa, Y., Fujiwara, H. & Sato, T. Photoelectric response of black lipid membranes incorporating an amphiphilic azobenzene derivative. *Thin Solid Films* **210/211**, 736–738 (1992).
8. Tanaka, M. & Yonezawa, Y. Photochemical regulation of ion transport through "quasi-channels" embedded in black lipid membrane. *Mat. Sci. Eng. C.* **4**, 297–301 (1997).
9. Garner, L. E. et al. Modification of the optoelectronic properties of membranes via insertion of amphiphilic phenylenevinylene oligoelectrolytes. *JACS* **132**, 10042–10052 (2010).
10. Hinks, J. et al. Modeling cell membrane perturbation by molecules designed for transmembrane electron transfer. *Langmuir* **30**, 2429–2440 (2014).
11. Gorostiza, P. & Isacoff, E. Optical switches and triggers for the manipulation of ion channels and pores. *Mol. Biosyst.* **3**, 686–704 (2007).
12. Fortin, D. L. et al. Photochemical control of endogenous ion channels and cellular excitability. *Nat. Methods* **5**, 331–338 (2008).
13. Kramer, R. H., Mourot, A. & Adesnik, H. Optogenetic pharmacology for control of native neuronal signaling proteins. *Nat. Neurosci.* **16**, 816–823 (2013).
14. Tochitsky, I., Kienzler, M. A., Isacoff, E. & Kramer, R. H. Restoring vision to the blind with chemical photoswitches. *Chem. Rev.* **118**, 10748–10773 (2018).
15. Laprell, L. et al. Restoring light sensitivity in blind retinae using a photochromic AMPA receptor agonist. *ACS Chem. Neurosci.* **7**, 15–20 (2016).
16. Laprell, L. et al. Photopharmacological control of bipolar cells restores visual function in blind mice. *J. Clin. Invest.* **127**, 2598–2611 (2017).
17. Ghezzi, D. et al. A hybrid bioorganic interface for neuronal photoactivation. *Nat. Commun.* **2**, 166 (2011).
18. Ghezzi, D. et al. A polymer optoelectronic interface restores light sensitivity in blind rat retinas. *Nat. Photonics* **7**, 400–406 (2013).
19. Feyen, P. et al. Light-evoked hyperpolarization and silencing of neurons by conjugated polymers. *Sci. Rep.* **6**, 22718 (2016).
20. Rand, D. et al. Direct electrical neurostimulation with organic pigment photocapacitors. *Adv. Mater.* **30**, e1707292 (2018).
21. Maya-Vetencourt, J. F. et al. A fully organic retinal prosthesis restores vision in a rat model of degenerative blindness. *Nat. Mater.* **16**, 681–689 (2017).
22. Martino, N. et al. Photothermal cellular stimulation in functional bio-polymer interfaces. *Sci. Rep.* **5**, 8911 (2015).
23. Lodola, F., Martino, N., Tullii, G., Lanzani, G. & Antognazza, M. R. Conjugated polymers mediate effective activation of the mammalian ion channel transient receptor potential vanilloid 1. *Sci. Rep.* **7**, 8477 (2017).
24. Shapiro, M. G., Homma, K., Villarreal, S., Richter, C. P. & Bezanilla, F. Infrared light excites cells by changing their electrical capacitance. *Nat. Commun.* **3**, 736 (2012).
25. Carvalho-de-Souza, J. L. et al. Photosensitivity of neurons enabled by cell-targeted gold nanoparticles. *Neuron* **86**, 207–217 (2015).
26. Bandara, H. M. & Burdette, S. C. Photoisomerization in different classes of azobenzene. *Chem. Soc. Rev.* **41**, 1809–1825 (2012).
27. Hartley, G. S. The *Cis*-form of azobenzene. *Nature* **140**, 281–281 (1937).
28. Rau, H. Spectroscopic properties of organic azo compounds. *Angew. Chem.* **12**, 224–235 (1973).
29. Tang B. Z. & Qin A. *Aggregation-Induced Emission: Fundamentals* (Wiley, 2013).
30. Sierocki, P. et al. Photoisomerization of azobenzene derivatives in nanostructured silica. *J. Phys. Chem. B* **110**, 24390–24398 (2006).
31. Fendler, J. H. Surfactant vesicles as membrane mimetic agents: characterization and utilization. *Acc. Chem. Res.* **13**, 7–13 (1980).
32. Head, B. P., Patel, H. H. & Insel, P. A. Interaction of membrane/lipid rafts with the cytoskeleton: impact on signaling and function: membrane/lipid rafts, mediators of cytoskeletal arrangement and cell signaling. *Biochim. Biophys. Acta* **1838**, 532–545 (2014).
33. Fruscione, F. et al. PRRT2 controls neuronal excitability by negatively modulating Na$^+$ channel 1.2/1.6 activity. *Brain* **141**, 1000–1016 (2018).
34. Thalhammer, A. et al. Alternative splicing of P/Q-type Ca^{2+} channels shapes presynaptic plasticity. *Cell Rep.* **20**, 333–343 (2017).
35. Zhang, Q. & Bazuin, C. G. Liquid crystallinity and other properties in complexes of cationic azo-containing surfactomesogens with poly(styrenesulfonate). *Macromolecules* **42**, 4775–4786 (2009).
36. Peddie, V., Anderson, J., Harvey, J. E., Smith, G. J. & Kay, A. Synthesis and solution aggregation studies of a suite of mixed neutral and zwitterionic chromophores for second-order nonlinear optics. *J. Org. Chem.* **79**, 10153–10169 (2014).
37. Allen, J. A., Halverson-Tamboli, R. A. & Rasenick, M. M. Lipid raft microdomains and neurotransmitter signalling. *Nat. Rev. Neurosci.* **8**, 128–140 (2007).
38. Frank, J. A., Franquelim, H. G., Schwille, P. & Trauner, D. Optical control of lipid rafts with photoswitchable ceramides. *J. Am. Chem. Soc.* **138**, 12981–12986 (2016).
39. Hodgkin, Al & Huxley, A. F. A quantitative description of membrane current and its application to conduction and excitation in nerve. *J. Physiol.* **117**, 500–544 (1952).
40. Tremere, L. A., Pinaud, R., Irwin, R. P. & Allen, C. N. Postinhibitory rebound spikes are modulated by the history of membrane hyperpolarization in the SCN. *Eur. J. Neurosci.* **28**, 1127–1135 (2008).

Methods

Synthesis and characterization of Ziapin2. The synthetic route consists of the reduction of the nitro group of the Disperse Orange 3 dye in amine, which is then alkylated with α,ω-dibromohexane and finally treated with pyridine to yield the terminated pyridinium bromide.

Unless otherwise stated, all chemicals and solvent were commercially available and used without further purification. Thin-layer chromatography was performed using silica gel on aluminium foil (Sigma Aldrich); ^1H and ^{13}C NMR spectra were collected with a Bruker ARX400. Mass spectroscopy was carried out with a Bruker Esquire 3000 plus.

4-[2-(4-aminophenyl)diazen-1-yl]aniline (1). A mixture of Disperse Orange 3 (Sigma Aldrich, 1.21 g, 5.0 mmol) and $Na_2S \cdot 9H_2O$ (3.60 g 15.0 mmol) dissolved in 100 mL of MeOH is refluxed overnight under stirring. Then the mixture is cooled to room temperature and the solvent is removed under reduced pressure. The resulting red powder is washed with DCM and Et_2O, the combined organic layers are collected and the solvent is evaporated under reduced pressure to give 540 mg of the desired product **1** as an orange powder in 51% yield.

^1H NMR: (400 MHz, DMSO) δ 7.56 (d, J = 8.82 Hz, 2H), 6.62 (d, J = 8.82 Hz, 2H), 5.70 (s, 4H)

4,4′-Bis-(N,N-di-ω-bromohexyl)diaminoazobenzene (Azo-Br4), Azo-Br1, Azo-Br2. 537 mg of product **1** (2.53 mmol) is stirred in 10 ml of previously degassed acetonitrile, then 2.20 g of K_2CO_3 (15.9 mmol) and 1.6 ml of 1,6-dibromohexane (10.4 mmol) are added dropwise to the reaction mixture and refluxed for 72 h while monitored by thin-layer chromatography. The reaction mixture is filtered, and the solid is washed three times with diethyl ether, ethylacetate and dichloromethane. The excess of dibromohexane is removed under reduced pressure (3×10^{-1} mbar) at 70 °C. The raw material is purified by flash chromatography with silica gel using hexane/Et_2O 3/1 as eluent to give 52 mg of 4,4′-Bis-(N,N-di-ω-bromohexyl) diaminoazobenzene (Azo-Br4, 2.4% yield); 32 mg of Azo-Br1 (2.8% yield) and 33 mg of Azo-Br2 (2.1% yield) are also recovered.

Azo-Br4. ^1H NMR: (400 MHz, DMSO) δ (ppm) 7.62 (d, J = 8.80 Hz, 4H), 6.72 (d, J = 8.80 Hz, 4H), 3.53 (t, 16H), 1.82 (m, 8H), 1.56 (m, -CH₂-,8H), 1.44 (m, -CH₂-,8H), 1.35 (m, -CH₂-, 8H); MS: 865 (M + H)⁺, 887 (M + Na)⁺

Azo-Br1. ^1H NMR: (400 MHz, DMSO) δ 7.63 (d, J = 8.80 Hz, 2H), 7.58 (d, J = 8.80 Hz, 2H), 6.77 (d, J = 8.80 Hz, 2H), 6.64 (d, J = 8.80 Hz, 2H), 6.21 (t, -NH, 1H), 3.54 (t, -N-CH₂-, 6H), 3.09 (m, CH₂-NH, 2H), 1.83-1.42 (m, 1 CH₂-, 6H); MS: 458 (M + H)⁺

Azo-Br2. ^1H NMR: (400 MHz, DMSO) δ (ppm) 7.63 (d, J = 8.80 Hz, 4H), 6.77 (d, J = 8.80 Hz, 2H), 6.72 (d, J = 8.80 Hz, 2H), 3.53 (t, -N-CH₂-, 8H), 3.35 (t, -CH₂-Br), 1.82-1.35 (m, -CH₂-, 24H); MS: 621 (M + H)⁺

1-{6-[(4-{2-[4-(azepan-1-yl) phenyl]diazen-1-yl}phenyl)[6-(pyridin-1-ium-1-yl) hexyl] amino] hexyl} pyridin-1-ium dibromide (Ziapin2). 12 mg of **Azo-Br2** are dissolved in 3 ml of pyridine and stirred at room temperature for 42 h. Then 3 ml of methanol are added and further stirred for 60 h. The excess of pyridine and methanol are removed from the reaction mixture under reduced pressure to give a solid in quantitative yield that is further washed with small portions of hexane.

^1H NMR: (400 MHz, DMSO) δ 9.09 (d, Pyr, 4H), 8.61 (t, Pyr, 2H), 8.16 (t, Pyr, 4H), 7.62 (d, J = 8.8 Hz, Ph, 4H), 6.78 (d, J = 8.8 Hz, Ph, 2H), 6.70 (d, J = 8.8 Hz, Ph, 2H), 4.60 (t, -CH₂-Pyr-, 4H), 3.54 (t, N-CH₂-, 4H), 2.97-1.24 (m, 24H). ^{13}C NMR: (400 MHz, DMSO) δ 150.29, 149.45, 145.97, 145.21, 143.00, 128.56, 124.38, 124.24, 111.65, 111.36, 61.22, 50.54, 49.50, 31.15, 27.27, 27.15, 26.75, 26.27, 25.86. MS: 618 (M -2Br)⁺

The chromatographic analysis of Ziapin2 was performed by means of a Waters HPLC system equipped with a Waters 600 Controller, a Waters 996 Photodiode Array Detector and a Jupiter 5 μ C18 300A Phenomenex column. The measurement was carried out using a gradient programme with 25% CH_3CN/75% H_2O (both HiPerSolv Chromanorm grade solvents from VWR Chemicals) initial eluent mixture for 5 min progressively modified into 100% CH_3CN over a total period of 25 min. The spectrum of the isolated compound absorbs at nearly 470 nm.

UV–Vis absorption measurements. For the UV–Vis absorption measurements, we used a Perkin Elmer Lambda 1050 spectrophotometer equipped with deuterium (180–320 nm) and tungsten (320–3300 nm) lamps and three detectors (photomultiplier 180–860 nm, InGaAs 860–1300 nm and PbS 1300–3300 nm). For further details, see Supplementary Information.

Photoluminescence measurements. The PL measurements in solution (25 μM in DMSO, water and SDS; 100 mM) were taken with a Horiba Nanolog Fluorometer equipped with a xenon lamp, two monochromators and two detectors (photomultiplier and InGaAs). Hek293 cells, used as a source of cell membranes, were obtained from ATCC. The emission of azobenzene in the membrane environment at 450 nm was elicited by using a CW diode laser (excitation energy

of 10 mW mm⁻², matching that of electrophysiology experiments). The emission was collected with an ×50 objective (Zeiss), filtered to remove the wavelength excitation and sent to the camera (Hamamatsu, acquisition time 100 ms). The system was illuminated for a shorter time (10 s) than the PL measurements in solution, to avoid cell damage. For further details see Supplementary Information.

MD simulations. All-atom MD simulations of Ziapin2 in *trans* and *cis* conformations in a model membrane bilayer of 1-palmitoyl-2-oleoyl-phosphatidylcholine (POPC) made of 160 lipid molecules (80 per leaflet) and water. A starting conformation for the bilayer in water was generated using pre-equilibrated lipid structures from the CHARMM-GUI web server[41]. All simulations were run with NAMD v2.12 code[42] using the CHARMM36 force field[43] and TIP3P model for water molecules. CHARMM-compatible topology and parameters for Ziapin2 were obtained using the CHARMM General Force Field (CGenFF), and atomic charges were calculated at the B3LYP/cc-pVTZ level. The total electrostatic charge of each system was neutralized by the addition of physiological concentrations of counter ions. The time step for integrating the equation of motion was 2 fs. Simulations were performed using periodic boundary conditions in the NPT ensemble, that is, at constant pressure (1 atm) and temperature (310 K), using a Langevin piston with a constant decay of 100 ps⁻¹ and an oscillation period of 200 fs and a Langevin thermostat with a damping constant of 5 ps⁻¹. Flexible unit cell was used with constant ratio in the *x*–*y* plane. Long-range electrostatic interactions were computed using the particle-mesh Ewald method, with a fourth-order spline and 1 Å grid spacing. The PC/water system was simulated for 30 ns to equilibrate, and then the following simulations were performed: three runs of spontaneous *trans* Ziapin2 insertion in the membrane (two for 175 ns and one for 300 ns); two runs of a single Ziapin2 in the membrane, one in *trans* and one in *cis* conformation (200 ns each); two runs each with four copies of Ziapin2 in the membrane, in *trans* and *cis* conformation (200 ns each); two runs each with eight copies of Ziapin2 in the membrane, in *trans* and *cis* conformation (200 ns each); one run with 16 copies of Ziapin2 in the membrane in *trans* conformation (200 ns). When multiple copies of Ziapin2 were considered, they were distributing symmetrically in the upper and in the lower leaflet, aligned with the respective lipid headgroups. For the *cis* systems, the initial positions were determined by aligning the pyridine branches with those of the *trans* molecules. To determine the free energy profile for moving Ziapin2 from bulk water into the PC bilayer, we integrated a set of mean force values (that is, minus the derivative of the free energy) calculated at 34 different positions of the molecule along the axis normal to the bilayer. The different values of the mean force were computed by restraining the centre of mass of the pyridine nitrogen atoms of Ziapin2 at positions spaced by 1 Å along the normal with a force constant of 100 kcal mol⁻¹ Å⁻². The centre of mass of the bilayer was kept fixed in all mean force simulations. At each position, the simulation lasted for 10–20 ns, until convergence of the mean force estimator was observed. To simulate the effect of light-induced *trans→cis* Ziapin2 conformational change on the membrane, we extracted a pinched bilayer conformation from the simulation with eight *trans* Ziapin2, deleted the photochromic molecules, inserted eight Ziapin2 in *cis* conformations and ran a standard MD trajectory for 200 ns. For further details on the raft simulations model[44] and MD technique[45], see Supplementary Information.

Atomic force microscopy. Atomic force microscopy data were acquired using an Oxford Instrument Cypher AFM equipped with a liquid droplet probe holder. AFM scans were acquired in liquid in AC mode (free amplitude ~6 nm) using BL-AC40TS cantilevers (Olympus), with a nominal resonance frequency in air of 110 kHz and a nominal spring constant of 0.09 N m⁻¹.

Liposomes were prepared as previously reported[46]. Bilayers were prepared starting from a 6 mg ml⁻¹ large unilamellar vesicles (LUV) solution in phosphate buffer (150 mM NaCl, 15 mM sodium phosphate, pH 7.4), exposed to Ziapin2 (2 mM in DMSO) for 7 min at room temperature, at a molar ratio lipid/Ziapin2 of around 50. In control experiments, we added to the LUV solution, instead of the Ziapin2 solution, the same volume of pure DMSO. Samples were then diluted in phosphate buffer at a final lipid concentration of 2 mg ml⁻¹ (PC bilayers) or of 1 mg ml⁻¹ (ternary membranes, PC:SM:Chol 1:1:1 (mol)) and supplemented with 1 mM $CaCl_2$ to help the vesicle fusion on the mica substrate. Supported lipid bilayers were deposited on freshly cleaved mica discs (Ted Pella), incubating for 10 min a 100 μl droplet of the LUV/Ziapin2 (LUV/DMSO) suspension. The excess of vesicles was removed by gently washing the samples with phosphate buffer. At least three samples for every condition were analysed. Data were imported in ImageJ for image plane fitting and line-by-line flattening, rendering and analysis.

Planar lipid bilayer experiments. Solvent-free planar lipid membranes were formed over a 100–180 μm diameter hole sparkling drilled in a 25-μm-thick Teflon septum, thus separating two compartments, as previously described[47]. Each chamber was filled with 2 mL buffer solution (150 mM NaCl, 15 mM sodium phosphate, pH 7.4), and stable bilayers were formed between the two chambers. Micromolar concentrations of Ziapin2 (5 μM) were sequentially added to the *cis* and to the *trans* sides of a stable preformed bilayer. Lipid compositions used were pure PC or PC:CHO:SM 57:33:10 (molar ratio). Currents were recorded with a patch-clamp amplifier (Axopatch 200B, Axon Instruments), and a PC equipped

with a DigiData 1550 A/D converter (Axon Instruments) was used for data acquisition. Current traces were filtered at 2 kHz and acquired at 10 kHz by the computer using Clampex 10.5 software (Axon Instruments). All measurements were performed in the dark at room temperature. Membrane capacitance was measured via continuous symmetrical triangular ramps (100 Hz in frequency), as summarized in Schmitt and Koepsell[48]. The membrane capacitance (C_m) is connected to the membrane characteristic features, for example area (A) and thickness (d), through the following equation (1):

$$C_m(pF) = A(nm^2) \in_r \in_0 (pF/nm)/d(nm) \quad (1)$$

For a stable membrane formed by a defined lipid class or composition, we can consider A and ϵ_r being constant for each experiment; therefore, a measured increase in the membrane capacitance reflects a linear reduction in the membrane thickness. The membrane capacitance (C_m) was obtained by subtracting the capacity of the septum, which is 30 pF in our conditions.

Electrophysiology. Whole-cell patch-clamp recordings of Hek293 cells and low-density primary hippocampal neurons (between 14 and 18 days in vitro) were performed at room temperature (22–24 °C) using 3–4 MΩ borosilicate patch pipettes (Kimble, Kimax, Mexico) and under GΩ patch seal. Cells with leak currents >200 pA or series resistance (R_s) >15 MΩ were discarded. The R_s was compensated 80% (2 μs response time), and the compensation was readjusted before stimulation. The shown potentials were not corrected for the measured liquid junction potential (9 mV). Voltage-clamp recordings were sampled at 20 kHz and low-pass filtered at 4 kHz. Current-clamp recordings were sampled at 50 kHz and low-pass filtered at 10 kHz. Patch-clamp recordings were carried out using either an Axopatch 200B (Molecular Devices, San José, CA) or an EPC10 (HEKA Elektronik, Reutlingen, Germany) amplifier.

For Hek293 cell recordings, patch electrodes (3–4 MΩ) were filled with an intracellular solution containing (in mM) 140 NaCl, 2 MgCl₂, 5 HEPES (pH 7.4). Cells were bathed during whole-cell recordings in an extracellular solution containing (in mM) 140 NaCl, 2 MgCl₂, 5 HEPES (pH 7.4) unless stated in the text. For recordings in primary neurons, the standard extracellular solution contained (in mM) 135 NaCl, 5.4 KCl, 1 MgCl₂, 1.8 CaCl₂, 5 HEPES, 10 glucose adjusted to pH 7.4 with NaOH. The standard intracellular solutions contained (in mM) 126 K-gluconate, 4 NaCl, 1 MgSO₄, 0.02 CaCl₂, 0.1 EGTA, 10 glucose, 5 HEPES, 3 ATP-Na₂, and 0.1 GTP-Na. When indicated, recordings were performed in the presence of the SB D-AP5 (50 μM)/CNQX (10 μM) and bicuculline (30 μM) (Tocris, Bristol, UK) to block excitatory and inhibitory synaptic transmission, respectively.

To investigate the contribution of ionic conductances in the capacitive currents evoked by light stimulation, the standard internal solution was used in combination with an extracellular solution where Na⁺ was replaced by choline or, alternatively, an 'external blocking solution' containing (in mM) NaCl 130, TEA Cl 3, CaCl₂ 1.8, MgCl₂ 1, CdCl₂ 5, NiCl₂ 1, GdCl₃ 1, HEPES 5, glucose 10, ouabain 1, in the presence of 30 μM tetrodotoxin, in combination with an 'internal blocking solution', containing (mM) CsMES 120, NaCl 4, CaCl₂ 0.02, EGTA 0.1, MgSO₄ 1, phosphocreatine 10, ATP-Na₂ 3, GTP-Na 0.1, HEPES 10. Solution exchange was performed using gravity flow controlled by pinch valves (Warner Instruments, Hamden, CT). All chemicals were purchased from Sigma Aldrich (St. Louis, MO, USA), except for tetrodotoxin from Tocris.

Capacitance recordings. Capacitance measurements were performed using the 'sine + dc' method[24,25,49] implemented as the 'sine 1 dc' feature of the PULSE lock-in module[50]. A sine wave function (1–5 mV peak-to-peak) was superimposed to the holding potential of −70 mV at a frequency of 150–300 Hz corresponding to the C_m sampling rates. To determine changes of membrane capacitance induced by light stimulation in Ziapin2-treated cells, the C_m was first averaged over 500 ms preceding the light stimulus and then subtracted from the peak value induced by the stimulation.

Equivalent circuit simulations. We numerically solved the equivalent circuit as shown in Supplementary Fig. 13, starting from the equilibrium position according to the input parameters $E = -60$ mV, starting capacity $C_m = 30$ pF, $1/g = 300$ MΩ. The resistor–capacitor (RC) time constant of the circuit is 90 μs. In the simulation, we changed C_m in time and calculated the predicted V_m by keeping g constant, according to the experimental observations.

Data analysis. Data were analysed using pCLAMP 10 or FitMaster v2x90.1, together with Prism 6.07 (GraphPad) and OriginPro 9 (OriginLab) softwares.
For further details, see Supplementary Information.

Photostimulation. Illumination of neurons during electrophysiological experiments for both Ziapin2 and ChETA was provided by an LED system (Lumencor Spectra X) fibre-coupled to an upright Nikon FN1 microscope. The light source emission peaked at 470 nm to match the Ziapin2 absorption spectrum and the power density of 20 mW mm⁻², as measured at the output of the microscope objective.

In vivo experiments. Surgery: Mice were anaesthetised with isoflurane and placed in a stereotaxic frame, where anaesthesia was maintained with an isoflurane flow. Ziapin2 (200 μM in 1 μl 10% DMSO in phosphate-buffered saline) or vehicle was injected with a 5 μl Hamilton syringe in the primary somatosensory cortex (S1ShNc) of the left hemisphere using the following stereotaxic coordinates: 2 mm anterior to lambda, 2 mm lateral to midline and −723 μm ventral to brain surface. Injection was done at a rate of 100 nl/min with a nano-jector (World Precision Instruments, Fl, USA). Five minutes after, to let the molecules diffuse within brain tissue, the craniotomy was extended by 1 mm laterally and 1 mm medially to accommodate the microwire array (16 electrodes in 2 rows of 8, 33 μm diameter, 250 μm pitch, 375 μm between rows (Tucker Davis Technologies)). The two central microwires were inserted at a depth of 723 μm, before being cleaned with saline and topped with silicone sealant (Kwik-cast, WPI). A hole was drilled 1 mm caudally to the injection hole, and a fibre optic cannula (MFC_400/430-0.66_10 mm_ZF1.25_FLT, Doric Lenses) was inserted at a depth of 1 mm and an angle of 65° from the vertical. Two surgical screws were inserted in the skull contralateral to the implants to be used as reference/ground for the microwires and support. The skull was then covered with dental cement, and diclofenac was systemically administered at a dose of 100 μl/20 g. In vivo recordings: For the evaluation of the acute effects of Ziapin2 loading, in vivo optical stimulations were performed in freely moving C57BL6 mice that had been previously injected with either DMSO ($N = 3$) or Ziapin2 ($N = 3$) and left to recover for 60 min before electrophysiological recordings. Light stimulation was delivered at 0.25 Hz with 40% jitter for either 20 or 200 ms at irradiances of 4, 25, 43 or 116 mW mm⁻² with a 473 nm laser (Shanghai Dream Lasers) to the freely moving rats. Each condition was repeated 25 times. Extracellular signals in response to stimulation were amplified, digitized and sampled at 1,017 Hz by commercially available hardware (System 3, Tucker-Davis Technologies) before being saved for offline analysis using custom Matlab scripts (The Mathworks). During acquisition, data were high-pass (1 Hz) and low-pass (100 Hz) filtered to extract LFPs. The peak amplitude of the LFP waves, recorded within the correct latency range after the light onset, was normalized by the averaged noise amplitude calculated from the non-responding channels over the same epoch. For the analysis of the persistence of the Ziapin2 effects over time, implanted C57BL6 mice that had been injected with either DMSO ($N = 3$) or Ziapin2 ($N = 4$) at time = 0 were photostimulated and recorded as described above 1, 4 and 7 d after Ziapin2 administration. Mice that received Ziapin2 injection, but were not implanted, were euthanized at the same times after the injection and the brain processed for Ziapin2 fluorescence microscopy and immunohistochemical analysis of astro- and micro-glial reaction.

For further details about numerical model of the PL signal dynamics in solution, total internal fluorescence microscopy, primary neuron preparations, differentiation of human neurons from induced pluripotent stem cells, cell viability assays, fluorescence imaging of the plasma membrane, Immunofluorescence staining and statistical analysis, see Supplementary Information.

Reporting Summary. Further information on research design is available in the Nature Research Reporting Summary linked to this article.

Data availability
The datasets generated and analysed during the current study are available from the corresponding author on reasonable request.

References
41. Jo, S., Kim, T., Iyer, V. G. & Im, W. CHARMM-GUI: a Web-based graphical user interface for CHARMM. *J. Comput. Chem.* **29**, 1859–1865 (2008).
42. Phillips, J. C. et al. Scalable molecular dynamics with NAMD +. *J. Comput. Chem.* **26**, 1781–1802 (2005).
43. Huang, J. & MacKerell, A. D. Jr. CHARMM36 all-atom additive protein force field: validation based on comparison to NMR data. *J. Comput. Chem.* **34**, 2135–2145 (2013).
44. Bennett, W. F. & Tieleman, D. P. Molecular simulation of rapid translocation of cholesterol, diacylglycerol, and ceramide in model raft and nonraft membranes. *J. Lipid Res.* **53**, 421–429 (2012).
45. Maragliano, L. & Vanden-Eijnden, E. A temperature accelerated method for sampling free energy and determining reaction pathways in rare events simulations. *Chem. Phys. Lett.* **426**, 168–175 (2006).
46. Dalla Serra, M. & Menestrina, G. Liposomes in study of pore-forming toxins. *Meth Enzymol.* **372**, 99–124 (2003).
47. Dalla Serra, M. & Menestrina, G. Characterization of molecular properties of pore-forming toxins with planar lipid bilayers. *Meth Mol. Biol.* **145**, 171–188 (2000).
48. Schmitt, B. M. & Koepsell, H. An improved method for real-time monitoring of membrane capacitance in *Xenopus laevis* oocytes. *Biophys. J.* **82**, 1345–1357 (2002).
49. Pusch, M. & Neher, E. Rates of diffusional exchange between small cells and a measuring patch pipette. *Pflug. Arch.* **411**, 204–211 (1988).
50. Gillis, K. D. Admittance-based measurement of membrane capacitance using the EPC-9 patch-clamp amplifier. *Pflug. Arch.* **439**, 655–664 (2000).

Author contributions

C.B. designed and engineered Ziapin2. S.C., L.C. and F.O. performed the synthesis and characterization of Ziapin2. D.F. calculated the atomic charges and optimized coordinates. G.M.P. performed the spectroscopic characterization. L.M. performed molecular dynamics simulations. M.D.S., L.L. and M.M. performed planar lipid membrane and AFM studies. M.B., G.G. and E.C. studied the in vitro and in vivo distribution of the Ziapin compounds in neurons. M.L.D.F., P.B., E.C. and F.L. performed the in vitro patch-clamp experiments and analysed the data. V.V. elaborated the numerical RC model. J.F.M-V., E.C., D.S. and C.G.E. performed and analysed the in vivo experiments. M.L.D.F., E.C., P.B., G.M.P. and F.L. contributed to paper writing. G.L., C.B. and F.B. conceived the work. G.L. and F.B. planned the experiments, analysed the data and wrote the manuscript.

Competing interests

The authors declare no competing interests.

Additional information

Supplementary information is available for this paper at https://doi.org/10.1038/s41565-019-0632-6.

Correspondence and requests for materials should be addressed to G.L. or F.B.

Peer review information *Nature Nanotechnology* thanks Or Shemesh, Joao L. Carvalho-de-Souza and the other, anonymous, reviewer(s) for their contribution to the peer review of this work.

Reprints and permissions information is available at www.nature.com/reprints.

nature research

Corresponding author(s):	DBPR - NNANO-18091898C
Last updated by author(s):	Dec 19, 2019

Reporting Summary

Nature Research wishes to improve the reproducibility of the work that we publish. This form provides structure for consistency and transparency in reporting. For further information on Nature Research policies, see Authors & Referees and the Editorial Policy Checklist.

Statistics

For all statistical analyses, confirm that the following items are present in the figure legend, table legend, main text, or Methods section.

n/a	Confirmed	
☐	☒	The exact sample size (n) for each experimental group/condition, given as a discrete number and unit of measurement
☐	☒	A statement on whether measurements were taken from distinct samples or whether the same sample was measured repeatedly
☐	☒	The statistical test(s) used AND whether they are one- or two-sided *Only common tests should be described solely by name; describe more complex techniques in the Methods section.*
☒	☐	A description of all covariates tested
☐	☒	A description of any assumptions or corrections, such as tests of normality and adjustment for multiple comparisons
☐	☒	A full description of the statistical parameters including central tendency (e.g. means) or other basic estimates (e.g. regression coefficient) AND variation (e.g. standard deviation) or associated estimates of uncertainty (e.g. confidence intervals)
☐	☒	For null hypothesis testing, the test statistic (e.g. F, t, r) with confidence intervals, effect sizes, degrees of freedom and P value noted *Give P values as exact values whenever suitable.*
☒	☐	For Bayesian analysis, information on the choice of priors and Markov chain Monte Carlo settings
☒	☐	For hierarchical and complex designs, identification of the appropriate level for tests and full reporting of outcomes
☒	☐	Estimates of effect sizes (e.g. Cohen's d, Pearson's r), indicating how they were calculated

Our web collection on statistics for biologists contains articles on many of the points above.

Software and code

Policy information about availability of computer code

Data collection	Molecular Dynamics simulations were performed using NAMD 2.12, developed and maintained by the Theoretical and Computational Biophysics Group (TCB) at the University of Illinois at Urbana–Champaign, available as freeware for research use. Planar lipid bilayer and patch-clamp recordings were carried out using either an Axopatch 200B (Molecular Devices, San José, CA) or an EPC10 (HEKA Elektronik, Reutlingen, Germany) amplifier and stored in Clampfit (Molecular Devices) or Patchmaster V2.73 (HEKA Elektronik), respectively. In vivo extracellular signals in response to stimulation were amplified, digitized and sampled at 1017 Hz by commercially available hardware (System 3, Tucker-Davis Technologies) before being saved for offline analysis using custom Matlab scripts (The Mathworks).
Data analysis	Molecular Dynamics simulations were analyzed using in-house scripting and VMD, developed and maintained by the Theoretical and Computational Biophysics Group (TCB) at the University of Illinois at Urbana–Champaign, available as freeware for research use. Electrophysiological data were analyzed using pCLAMP 10 or FitMaster v2x90.1, together with Prism 6.07 (GraphPad) and OriginPro 9 (OriginLab) softwares.

For manuscripts utilizing custom algorithms or software that are central to the research but not yet described in published literature, software must be made available to editors/reviewers. We strongly encourage code deposition in a community repository (e.g. GitHub). See the Nature Research guidelines for submitting code & software for further information.

Data

Policy information about availability of data

All manuscripts must include a data availability statement. This statement should provide the following information, where applicable:

- Accession codes, unique identifiers, or web links for publicly available datasets
- A list of figures that have associated raw data
- A description of any restrictions on data availability

The data that support the findings of this study are available from the corresponding authors upon reasonable request.

Field-specific reporting

Please select the one below that is the best fit for your research. If you are not sure, read the appropriate sections before making your selection.

☒ Life sciences ☐ Behavioural & social sciences ☐ Ecological, evolutionary & environmental sciences

For a reference copy of the document with all sections, see nature.com/documents/nr-reporting-summary-flat.pdf

Life sciences study design

All studies must disclose on these points even when the disclosure is negative.

Sample size	The size of the experimental groups (n) has been calculated by using the following formula: $n = Z^2 * \sigma^2 / \Delta^2$ where: Z = 2.8 (from a Type I error α = 0.05 / Type II error β = 0.20); σ = standard deviation (25%, calculated from preliminary data); Δ = the minimum detectable percent difference between groups (20%) (Krzywinski M & Altman N, Power and sample size. Nat. Meth. 10:1139-1140, 2013)
Data exclusions	No data were excluded.
Replication	All findings were done in replicates from independent samples.
Randomization	Allocation was random
Blinding	The investigators were blinded to group allocation during data analysis.

Reporting for specific materials, systems and methods

We require information from authors about some types of materials, experimental systems and methods used in many studies. Here, indicate whether each material, system or method listed is relevant to your study. If you are not sure if a list item applies to your research, read the appropriate section before selecting a response.

Materials & experimental systems

n/a	Involved in the study
☐	☒ Antibodies
☐	☒ Eukaryotic cell lines
☒	☐ Palaeontology
☐	☒ Animals and other organisms
☒	☐ Human research participants
☒	☐ Clinical data

Methods

n/a	Involved in the study
☒	☐ ChIP-seq
☒	☐ Flow cytometry
☒	☐ MRI-based neuroimaging

Antibodies

Antibodies used	Chicken monoclonal anti-β-tubulin III, #302-306, Synaptic Systems Mouse monoclonal anti-glial fibrillary protein (GFAP) #G3893, Sigma-Aldrich Rabbit polyclonal anti-microglia specific protein (Iba1), #016-20001, Wako Fluorescently conjugated secondary antibodies were from Molecular Probes (Thermo-Fisher Scientific; Alexa Fluor 488, #A11029; Alexa Fluor 568, #A11036; Alexa Fluor 647, #A21450)
Validation	The primary antibodies were validated by the manufacturer and their specificity described in the data sheets and the manufacturer's website.

Eukaryotic cell lines

Policy information about cell lines

Cell line source(s)	HEK-293, human-Induced pluripotent stem cells derived neurons.
Authentication	The cell line was not authenticated.
Mycoplasma contamination	Negative for mycoplasma
Commonly misidentified lines (See ICLAC register)	No misidentified cell lines were used.

Animals and other organisms

Laboratory animals	C57BL6/J mice (Charles River).
Wild animals	N/A
Field-collected samples	N/A
Ethics oversight	All animal manipulations and procedures were performed in accordance with the guidelines established by the European Community Council (Directive 2010/63/EU of March 4th 2014) and were approved by the Institutional Ethics Committee and by the Italian Ministry of Health.

Note that full information on the approval of the study protocol must also be provided in the manuscript.